

## Supporting Information

# Reversible phenol oxidation-reduction in the structurally well-defined 2-mercaptophenol- $\alpha_3$ C protein

*Cecilia Tommos,\* Kathleen G. Valentine, Melissa C. Martínez-Rivera,*

*Li Liang and Veronica R. Moorman*

Graduate Group in Biochemistry & Molecular Biophysics and Department of Biochemistry & Biophysics, University of Pennsylvania, Philadelphia, Pennsylvania 19104-6059

tommos@mail.med.upenn.edu

Index	page
Table S1. Guide correlating the residue and atom designations used for 2MP-C32	S2
Table S2. Helical regions, $^3J_{\text{HNHA}}$ coupling constants and RCI values for 2MP- $\alpha_3$ C	S3
Table S3. Solvent accessible surface area analysis of the 2MP- $\alpha_3$ C structure	S4
Table S4. Solvent accessible surface area analysis of the 2MP- $\alpha_3$ C structure	S5
Optimizing the Faradaic current of 2MP- $\alpha_3$ C on a PGE working electrode	S6–S7
Figure S1. 2MP- $\alpha_3$ C/PGE electrode optimization and controls	S6
Figure S2. Raw square-wave voltammograms of 2MP- $\alpha_3$ C, $\alpha_3$ C and buffer samples	S7
2MP- $\alpha_3$ C exhibits diffusion-controlled kinetics on a PGE electrode	S7
2MP- $\alpha_3$ C/PGE electrode SWV error analysis	S7–S9
Figure S3. Representative 2MP- $\alpha_3$ C raw and processed square-wave voltammograms	S8
Figure S4. 2MP- $\alpha_3$ C square-wave voltammograms are highly reproducible	S8–S9
Figure S5. Determination of the 2MP- $\alpha_3$ C diffusion coefficient	S9
References	S10

<b>Residue RCSB PDB</b>	<b>Residue BMRB</b>	<b>Residue (this study)</b>	<b>Atoms RCSB PDB</b>	<b>Atoms BMRB</b>	<b>Atoms (this study)</b>
CYS-34	CYS-34	2MP-C32	N	N	backbone N
CYS-34	CYS-34	2MP-C32	H	H	backbone H
CYS-34	CYS-34	2MP-C32	C	C	backbone C
CYS-34		2MP-C32	O		backbone O
CYS-34	CYS-34	2MP-C32	CA	CA	backbone CA
CYS-34	CYS-34	2MP-C32	HA	HA	backbone HA
CYS-34	CYS-34	2MP-C32	CB	CB	sidechain CB
CYS-34	CYS-34	2MP-C32	HB2	HB2	sidechain HB2
CYS-34	CYS-34	2MP-C32	HB3	HB3	sidechain HB3
CYS-34		2MP-C32	SG		sidechain SG
HTS-101		2MP-C32	S1		sidechain phenol S
HTS-101		2MP-C32	C2		sidechain phenol C2
HTS-101		2MP-C32	C3		sidechain phenol C3
HTS-101	HTS-101	2MP-C32	H3	H3	sidechain phenol H3
HTS-101		2MP-C32	C4		sidechain phenol C4
HTS-101	HTS-101	2MP-C32	H4	H4	sidechain phenol H4
HTS-101		2MP-C32	C5		sidechain phenol C5
HTS-101	HTS-101	2MP-C32	H5	H5	sidechain phenol H5
HTS-101		2MP-C32	C6		sidechain phenol C6
HTS-101	HTS-101	2MP-C32	H6	H6	sidechain phenol H6
HTS-101		2MP-C32	C1		sidechain phenol C1
HTS-101		2MP-C32	O1		sidechain phenol O
HTS-101		2MP-C32	HO1		sidechain phenol H

**Table S1.** Designation for the modified cysteine/phenol residue in 2-mercaptophenol- $\alpha_3C$  used in the RCSB Protein Data Bank, the Biological Magnetic Resonance Bank (BMRB), and in this study. The convention used in the public databases requires that the attached phenol be labeled as a ligand with the name of HTS and a sequence residue number of 101. The nomenclature used in this study is based on treating the modified residue as a tyrosine analogue and labels the attached phenol as an extended sidechain of the single cysteine in 2MP- $\alpha_3C$ . Figure 4 in the main text displays the structure of the 2-mercaptophenol-C32 residue and the names of its associated atoms.

Residue	Helix	$J$ (Hz) <sup>a</sup>	RCI <sup>b</sup>	Residue	Helix	$J$ (Hz) <sup>a</sup>	RCI <sup>b</sup>
-2 GLY				32 2MP-C	helix 2	3.47	0.015
-1 SER				33 GLU	helix 2	4.10	0.015
1 ARG			0.039	34 GLU	helix 2	4.46	0.015
2 VAL	helix 1	6.12	0.039	35 LEU	helix 2	5.18	0.017
3 LYS	helix 1	4.06	0.036	36 LYS	helix 2	3.52	0.017
4 ALA	helix 1	3.75	0.031	37 LYS	helix 2	4.95	0.018
5 LEU	helix 1	5.80	0.023	38 LYS	helix 2	4.14	0.018
6 GLU	helix 1	3.71	0.018	39 ILE	helix 2	4.56	0.020
7 GLU	helix 1	4.44	0.017	40 GLU	helix 2	4.19	0.031
8 LYS	helix 1	4.40	0.018	41 GLU	helix 2	6.50	0.0101
9 VAL	helix 1	5.15	0.020	42 LEU		4.58	0.110
10 LYS	helix 1	4.16	0.024	43 GLY			0.181
11 ALA	helix 1	4.62	0.024	44 GLY			0.286
12 LEU	helix 1	4.64	0.021	45 GLY			0.385
13 GLU	helix 1	3.06	0.016	46 GLY			0.324
14 GLU	helix 1	3.86	0.015	47 GLU		6.33	0.189
15 LYS	helix 1	4.32	0.017	48 VAL	helix 3	4.50	0.049
16 VAL	helix 1	4.75	0.020	49 LYS	helix 3	3.20	0.028
17 LYS	helix 1	3.60	0.040	50 LYS	helix 3	5.19	0.021
18 ALA		6.08	0.117	51 VAL	helix 3	5.72	0.017
19 LEU		6.17	0.175	52 GLU	helix 3	3.35	0.015
20 GLY			0.186	53 GLU	helix 3		0.014
21 GLY			0.128	54 GLU	helix 3	4.95	0.014
22 GLY			0.083	55 VAL	helix 3	4.58	0.015
23 GLY			0.062	56 LYS	helix 3	3.71	0.019
24 ARG	helix 2	5.04	0.046	57 LYS	helix 3	3.96	0.020
25 ILE	helix 2	5.56	0.029	58 LEU	helix 3	4.70	0.020
26 GLU	helix 2	3.75	0.020	59 GLU	helix 3	3.35	0.016
27 GLU	helix 2	4.16	0.016	60 GLU	helix 3	4.61	0.015
28 LEU	helix 2	4.95	0.015	61 GLU	helix 3	4.79	0.017
29 LYS	helix 2	3.10	0.014	62 ILE	helix 3	4.38	0.025
30 LYS	helix 2	4.75	0.015	63 LYS	helix 3	4.49	0.039
31 LYS	helix 2	4.46	0.015	64 LYS	helix 3	7.45	0.058
				65 LEU		6.49	0.067

**Table S2.** Correlation between helical regions in 2MP- $\alpha_3$ C as determined by MOLMOL (S1), (a) three-bond  $J_{\text{HNHA}}$  coupling constants (S2) and (b) Random Coils Index (RCI) values (S3).

Residue	Heptad Position	Average SASA (%)	Residue	Heptad Position	Average SASA (%)
-2 GLY		63.4 ± 9.7	32 2MP-C	<i>a</i>	<b>3.5 ± 0.7</b>
-1 SER		37.4 ± 6.6	33 GLU	<i>b</i>	29.8 ± 2.3
1 ARG	<i>g</i>	45.6 ± 8.3	34 GLU	<i>c</i>	26.1 ± 4.4
2 VAL	<i>a</i>	<b>11.4 ± 5.1</b>	35 LEU	<i>d</i>	<b>0.3 ± 0.5</b>
3 LYS	<i>b</i>	46.1 ± 3.5	36 LYS	<i>e</i>	18.1 ± 3.0
4 ALA	<i>c</i>	17.6 ± 4.3	37 LYS	<i>f</i>	39.8 ± 2.4
5 LEU	<i>d</i>	<b>2.6 ± 1.9</b>	38 LYS	<i>g</i>	17.4 ± 4.1
6 GLU	<i>e</i>	21.3 ± 3.7	39 ILE	<i>a</i>	<b>1.7 ± 0.9</b>
7 GLU	<i>f</i>	36.3 ± 3.9	40 GLU	<i>b</i>	46.9 ± 3.1
8 LYS	<i>g</i>	31.6 ± 4.7	41 GLU	<i>c</i>	40.6 ± 3.2
9 VAL	<i>a</i>	<b>0.0 ± 0.0</b>	42 LEU	<i>d</i>	<b>7.4 ± 1.4</b>
10 LYS	<i>b</i>	39.9 ± 3.7	43 GLY		32.4 ± 4.5
11 ALA	<i>c</i>	24.4 ± 3.0	44 GLY		31.9 ± 6.5
12 LEU	<i>d</i>	<b>3.9 ± 1.6</b>	45 GLY		32.1 ± 7.9
13 GLU	<i>e</i>	<b>12.1 ± 2.6</b>	46 GLY		34.2 ± 5.6
14 GLU	<i>f</i>	41.8 ± 2.9	47 GLU	<i>g</i>	31.3 ± 5.3
15 LYS	<i>g</i>	34.9 ± 6.8	48 VAL	<i>a</i>	<b>3.8 ± 3.4</b>
16 VAL	<i>a</i>	<b>0.8 ± 0.6</b>	49 LYS	<i>b</i>	46.9 ± 5.8
17 LYS	<i>b</i>	41.1 ± 2.4	50 LYS	<i>c</i>	39.5 ± 3.0
18 ALA	<i>c</i>	41.0 ± 0.9	51 VAL	<i>d</i>	<b>0.2 ± 0.4</b>
19 LEU	<i>d</i>	<b>21.1 ± 2.7</b>	52 GLU	<i>e</i>	17.2 ± 5.4
20 GLY		30.7 ± 6.7	53 GLU	<i>f</i>	39.8 ± 2.9
21 GLY		33.0 ± 3.4	54 GLU	<i>g</i>	13.5 ± 3.5
22 GLY		26.9 ± 7.2	55 VAL	<i>a</i>	<b>1.4 ± 1.1</b>
23 GLY		26.2 ± 4.3	56 LYS	<i>b</i>	40.2 ± 5.0
24 ARG	<i>g</i>	30.9 ± 4.1	57 LYS	<i>c</i>	33.6 ± 3.2
25 ILE	<i>a</i>	<b>4.7 ± 2.1</b>	58 LEU	<i>d</i>	<b>0.1 ± 0.2</b>
26 GLU	<i>b</i>	37.8 ± 4.5	59 GLU	<i>e</i>	17.8 ± 3.7
27 GLU	<i>c</i>	35.6 ± 4.4	60 GLU	<i>f</i>	41.4 ± 3.2
28 LEU	<i>d</i>	<b>0.1 ± 0.1</b>	61 GLU	<i>g</i>	13.1 ± 5.3
29 LYS	<i>e</i>	29.5 ± 5.2	62 ILE	<i>a</i>	<b>2.3 ± 1.5</b>
30 LYS	<i>f</i>	47.4 ± 4.0	63 LYS	<i>b</i>	42.3 ± 3.0
31 LYS	<i>g</i>	9.7 ± 2.3	64 LYS	<i>c</i>	54.6 ± 4.6
			65 LEU	<i>d</i>	<b>24.8 ± 3.9</b>

**Table S3.** Average solvent accessible surface areas (SASA) of residues in 2MP- $\alpha_3$ C. The SASA analysis was performed on the 32-membered structural ensemble that represents the solution NMR structure of 2MP- $\alpha_3$ C using MOLMOL (S1). A solvent probe radius of 1.4 Å and a level 5 precision were used for the calculations. The solvent accessible surface area (%) is defined as the percentage ratio of the water-accessible surface area of the listed residue X to the accessible surface area of the same residue placed in a Gly-X-Gly peptide. The average SASA of residues placed in heptad a and d positions are shown in red. The average SASA of the hydrogen-bonded 2MP-C32 and E13 pair are shown in blue.

Residue	Atoms	Average SASA (%)	SASA limits (%)
2MP-C32	backbone N, H, C, O, CA	0 ± 0	0
2MP-C32	backbone HA	0.1 ± 0.3	0.0 – 1.6
2MP-C32	sidechain CB, HB2, HB3, SG	0 ± 0	0
2MP-C32	sidechain phenol S	0 ± 0	0
2MP-C32	sidechain phenol C2, C3, H3, C4	0 ± 0	0
2MP-C32	sidechain phenol H4	0.3 ± 0.8	0.0 – 4.2
2MP-C32	sidechain phenol C5	4.5 ± 3.1	0.0 – 11.0
2MP-C32	sidechain phenol H5	10.2 ± 8.1	0.0 – 31.3
2MP-C32	sidechain phenol C6	4.7 ± 1.8	0.5 – 8.2
2MP-C32	sidechain phenol H6	38.2 ± 5.7	22.7 – 47.5
2MP-C32	sidechain phenol C1	0 ± 0	0
2MP-C32	sidechain phenol O	2.0 ± 3.1	0 – 12.3
2MP-C32	sidechain phenol H	4.0 ± 5.4	0 – 20.3
2MP-C32	all atoms	3.5 ± 0.7	2.0 – 5.4
E13	backbone N, H, C, O, CA, HA	0 ± 0	0
E13	sidechain CB, HB2, CG	0 ± 0	0
E13	sidechain HB3	1.0 ± 1.6	0 – 5.6
E13	sidechain HG2	8.1 ± 7.1	0 – 23.4
E13	sidechain HG3	0.3 ± 1.2	0 – 6.4
E13	sidechain CD	17.2 ± 17.6	0 – 52.5
E13	sidechain OE1	37.4 ± 18.3	6.5 – 69.6
E13	sidechain OE2	35.9 ± 18.7	9.0 – 80.5
E13	all atoms	12.1 ± 2.6	6.5 – 16.9

**Table S4.** Solvent accessible surface areas (SASA) of atoms associated with the 2-mercaptophenol-C32 (2MP-C32) and E13 residues. The analysis was performed as described in the legend to Table S3.

**Optimizing the Faradaic current of 2MP- $\alpha_3$ C on a PGE working electrode.** The square-wave voltammetry (SWV; S4-S6) analysis of 2MP- $\alpha_3$ C required a pyrolytic graphite “edge” (PGE) working electrode in order to generate good signal-to-noise data. A set of experiments was conducted to optimize and characterize the 2MP- $\alpha_3$ C/PGE electrode system. The interactions between the protein surface (mainly carboxyl and amine groups from Glu and Lys residues) and the PGE electrode surface (rich in acidic C–O groups; S7, S8) are likely to be dominated by electrostatics. The sample KCl concentration was consequently an important parameter to consider when optimizing the Faradaic current. In addition, it was important to establish that chemical groups present at the surface of the PGE electrode do not influence the observed phenol potential. **Figure S1A** shows the 2MP- $\alpha_3$ C differential pulse voltammetry (DPV; S4, S9)  $E_{1/2}$  potential as a function of [KCl] at pH 5.6 (red) and 7.7 (blue). The data were collected with 40 mM buffer present in the sample and using a slow scan rate of 9 mV s<sup>-1</sup>, as described in the figure legend. At low pH the observed potential is independent of [KCl] with an average  $E_{1/2}$ (pH 5.61) of 1003 ± 2 mV across the 0 – 140 mM range. At high pH a very weak influence on  $E_{1/2}$  is observed at low KCl concentrations.  $E_{1/2}$ (pH 7.70) decreases by 5 ± 1 mV between 0 and 40 mM KCl and then levels out at 884 ± 1 mV for the 40 – 140 mM range. The half-height peak width was found to be independent on [KCl] and remained at 103 ± 3 mV (pH 5.6) and 118 ± 5 mV (pH 7.7) between 0 – 140 mM KCl. In contrast, the current amplitude decreases by ~ 60% between 0 and 140 mM KCl at both high and low pH and continues to decline at higher KCl concentrations (data not shown). From these results we conclude that there are favorable electrostatic interactions between the protein and the PGE surface at pH ≤ 7.7 and that the strength of these interactions decreases as [KCl] increases. This is consistent with a positively charged protein (calculated isoelectric point ~ 9) and a negatively charged PGE electrode surface (S7, S8). We conclude that  $E_{1/2}$  is not influenced by chemical groups present at the PGE electrode surface at KCl concentrations above 40 mM and that 40 – 140 mM KCl represents an optimized range.

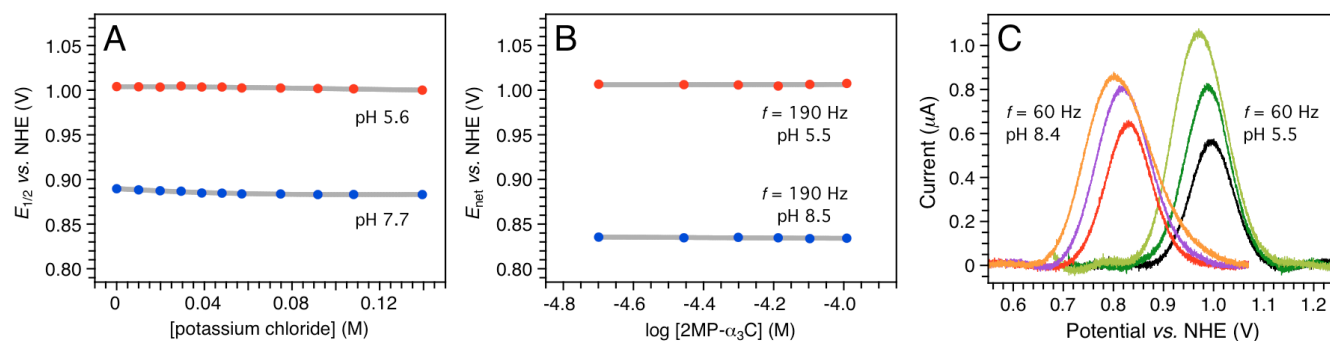


**Figure S1.** 2MP- $\alpha_3$ C/PGE electrode optimization and controls. (A) 2MP- $\alpha_3$ C DPV  $E_{1/2}$  as a function of [KCl] at pH 5.61 ± 0.01 (red circles) and pH 7.70 ± 0.01 (blue circles). DPV settings: 30  $\mu$ M 2MP- $\alpha_3$ C in 20 mM sodium acetate and 20 mM potassium phosphate (pH 5.61 ± 0.01); 20  $\mu$ M 2MP- $\alpha_3$ C in 20 mM potassium phosphate and 20 mM sodium borate (7.70 ± 0.01); PGE working electrode, temperature 25° C, interval time 0.1 s, step potential 0.9 mV, scan rate 9.0 mV s<sup>-1</sup>, modulation time 7 or 8 ms, modulation amplitude 50 mV. (B) 2MP- $\alpha_3$ C SWV  $E_{net}$  as a function of the sample protein concentration at pH 5.54 ± 0.02 (red circles) and pH 8.55 ± 0.02 (blue circles). SWV settings: 2MP- $\alpha_3$ C in 20 mM APB, 80 mM KCl; PGE working electrode, temperature 25° C, step potential 0.15 mV, SW pulse amplitude 25 mV, SW frequency 190 Hz. (C) Net 2MP- $\alpha_3$ C voltammograms recorded using a SW frequency of 60 Hz and a pulse amplitude between 25 and 75 mV. The figure displays two data sets collected at pH 5.55 ± 0.02 and 8.43 ± 0.02. The SW pulse amplitude was 25 mV (red and black), 50 mV (blue and medium green) and 75 mV (orange and light green). SWV settings: 75  $\mu$ M 2MP- $\alpha_3$ C in 20 mM APB, 80 mM KCl; PGE working electrode, temperature 25° C, step potential 0.15 mV, and SW frequency 60 Hz.

**Figure S1B** shows  $E_{net}$  as a function of [2MP- $\alpha_3$ C] at pH 5.5 (red) and 8.5 (blue). The SW voltammograms were collected on samples containing 20 mM sodium acetate, 20 mM potassium phosphate, 20

mM sodium borate (APB buffer), 80 mM KCl and 20 to 100  $\mu$ M protein.  $E_{\text{net}}$  shows no dependence on  $[2\text{MP-}\alpha_3\text{C}]$  and average values of  $1006 \pm 1$  mV (pH 5.54; 190 Hz) and  $834 \pm 1$  mV (pH 8.55; 190 Hz) were observed across the 20 – 100  $\mu$ M protein range. At both pH 5.5 and 8.5, the half-height peak width of the 2MP- $\alpha_3$ C net voltammogram remained at  $109 \pm 5$  mV while the amplitude increased by  $\sim 50\%$  as  $[2\text{MP-}\alpha_3\text{C}]$  was increased from 20 to 100  $\mu$ M (data not shown). The amplitude of the 2MP- $\alpha_3$ C SW voltammogram declines at protein concentrations above and below this range. We conclude that samples containing 20 mM APB, 40 – 140 mM KCl and 20 – 100  $\mu$ M protein generate SW voltammograms with optimal S/N. Two additional key observations can be made from **Fig. S1B**.  $E_{\text{net}}$  is not perturbed by any distorting interactions between the protein and the electrode surface nor influenced by intermolecular radical-radical or radical-substrate reactions. Such events depend on the protein concentration and would result in an  $\delta E_{\text{net}}/\delta \log[2\text{MP-}\alpha_3\text{C}] \neq 0$ . This is not observed. Thus, the protein does not unfold on the electrode surface and the oxidized protein is not involved in dimerization reactions. **Figure S2** shows raw SW voltammograms from 2MP- $\alpha_3$ C,  $\alpha_3$ C and buffer samples recorded at the conditions optimized for the PGE electrode. The Faradaic current observed from 2MP- $\alpha_3$ C (blue traces) is absent in the voltammograms recorded from the  $\alpha_3$ C (red) and buffer (green) samples. We further note that the S–S bond that ligates the phenol to the protein is not involved in the high-potential redox reactions probed here ( $E_{\text{m}} \text{ CSSC/CSH} < 0$  V; *S10*, *S11*). The Faradaic current of 2MP- $\alpha_3$ C is unambiguously assigned to the protein-bound phenol, as concluded earlier from DPV-based studies (*S10*, *S12*).

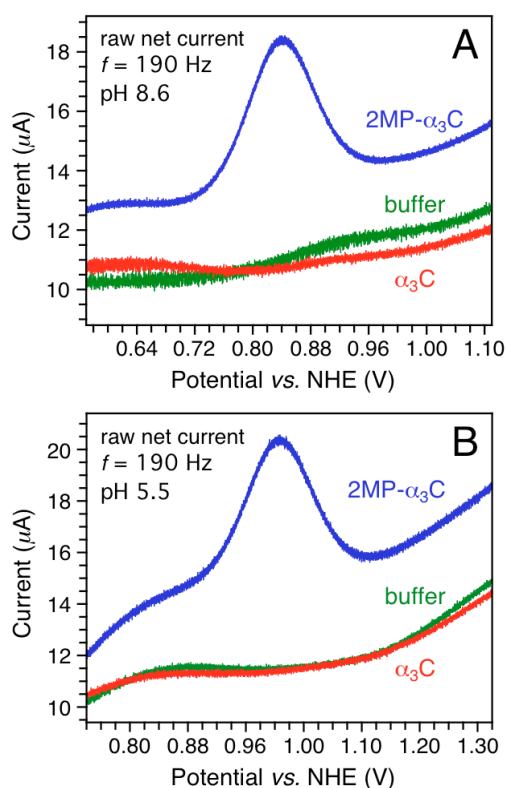


**Figure S2.** Raw square-wave voltammograms of 2MP- $\alpha_3$ C (blue),  $\alpha_3$ C (red) and plain buffer (green) obtained at (A) pH 8.5 and (B) pH 5.5. The 2MP- $\alpha_3$ C and  $\alpha_3$ C traces were obtained at 75  $\mu$ M protein. All samples contained 20 mM APB and 80 mM KCl. SWV settings: PGE working electrode, temperature 25° C, step potential 0.15 mV, SW pulse amplitude 25 mV, and SW frequency 190 Hz.

**2MP- $\alpha_3$ C exhibits diffusion-controlled kinetics on a PGE electrode.** Once optimal sample conditions had been established for the 2MP- $\alpha_3$ C/PGE working electrode system, data were collected to investigate whether adsorption or diffusion-controlled electrode kinetics occur at these conditions. Voltammograms representing a surface-confined redox species are influenced by the SW frequency and the pulse amplitude relative to the heterogeneous electron-transfer rate constant of the system (*S6*, *S13*). A combination of low frequencies and large pulse amplitudes may result in a splitting of the peak maximum in the net voltammogram. The splitting of the net peak provides a criterion for distinguishing a surface process from a diffusion-controlled electrode process (*S6*, *S13*). Square-wave voltammograms were collected at 60 Hz using a pulse

amplitude of 25, 50 and 75 mV. Data were collected at both pH 5.5 and 8.4, as shown in **Figure S1C**. The 2MP- $\alpha_3$ C net voltammogram shifts and becomes broader when applying an overpotential of 50 or 75 mV but there is no indication of a flattening or splitting of the peak maximum. The lineshape of the 2MP- $\alpha_3$ C net voltammogram as a function of pulse amplitude is consistent with diffusion-controlled electrode kinetics at both acidic and alkaline pH.

**2MP- $\alpha_3$ C/PGE electrode SWV error analysis.** **Figure S3A, B and C** show raw and background-corrected 2MP- $\alpha_3$ C SW voltammograms collected at 30 ( $t_p$  16.7 ms), 190 ( $t_p$  2.6 ms) and 540 ( $t_p$  926  $\mu$ s) Hz, respectively. Panels (A) and (B) display the raw net (blue), forward (orange) and reverse (purple) square-wave voltammograms with the fitted cubic baselines (---) that were used to generate the background-corrected traces shown in the middle of each data panel. The black solid lines (—) plotted on top of the background-corrected voltammograms represent fitted calculated lineshapes from which peak po-



tentials, peak amplitudes and half-height peak widths were extracted. The S/N of the 2MP- $\alpha_3$ C voltammogram is sensitive to the SW frequency and electric noise becomes more pronounced at higher frequencies. The traces obtained at 540 Hz (panel C) were first smoothened using a Savitzky-Golay algorithm (smooth level 0.2% for the net trace and 0.5% for the forward and reverse traces) and then processed as the 30 and 190 Hz data.

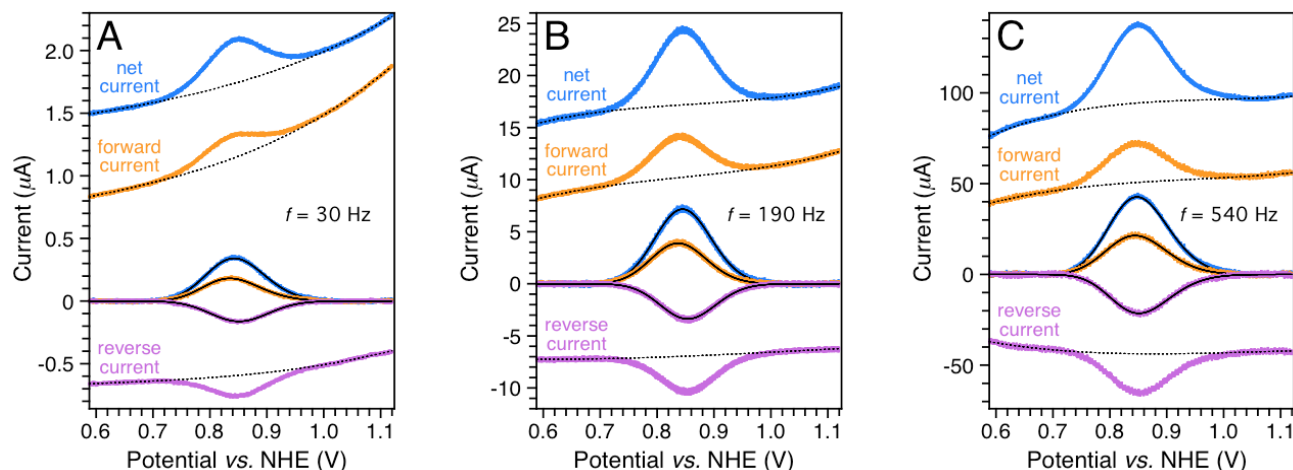


**Figure S3.** Representative 2MP- $\alpha_3$ C raw and background-corrected square-wave voltammograms. Settings: 75  $\mu$ M 2MP- $\alpha_3$ C in 20 mM APB, 80 mM KCl, pH 8.5; PGE working electrode, temperature 25 $^{\circ}$  C, step potential 0.15 mV, SW pulse amplitude 25 mV.

The **top row** in **Figure S4** displays a typical SWV raw data triplicate where panel (A) shows  $I_{\text{net}}$ , panel (B)  $I_{\text{for}}$  and panel (C)  $I_{\text{rev}}$ . The black and light blue traces displayed in the **bottom row** of **Figure S4** represent background-corrected 2MP- $\alpha_3$ C SW voltammograms obtained from two independent measurements. The high level of reproducibility illustrated in Fig. S4 was typical of SW voltammograms obtained from 2MP- $\alpha_3$ C at both acidic and alkaline pH. The average errors in  $E_{\text{peak}}$  ( $\leq \pm 5$  mV) and half-height peak widths ( $\leq \pm 5$  mV) were small. The peak amplitude and the S/N are both sensitive to the SW frequency with a small Faradaic current at low frequencies ( $\leq 60$  Hz) and an increase in noise at high frequencies ( $\geq 540$  Hz). The average error in  $I_{\text{net}}$  was about  $\pm 10\%$ .

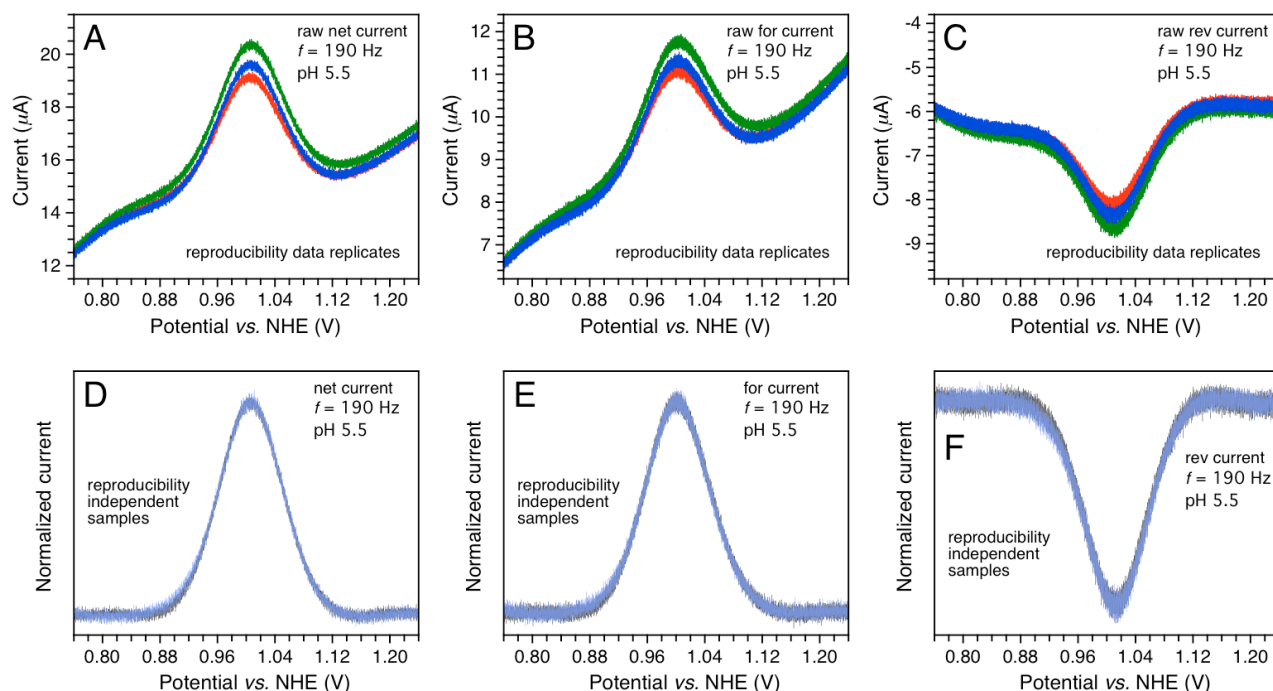




**Figure S4.** Typical reproducibility observed for (top row) data replicates and (bottom row) independent SWV measurements. Settings: 75  $\mu\text{M}$  2MP- $\alpha_3\text{C}$  in 20 mM APB, 80 mM KCl; PGE working electrode, temperature 25° C, step potential 0.15 mV, SW pulse amplitude 25 mV, SW frequency 190 Hz.

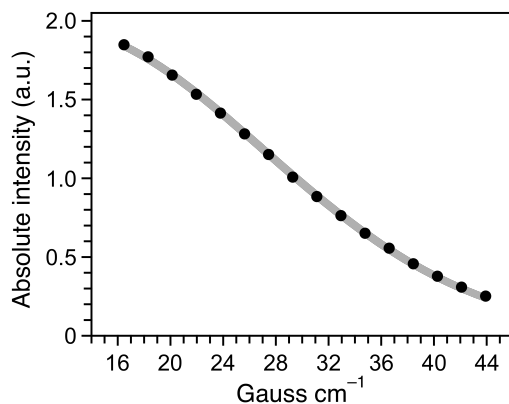


**Figure S5.** Diffusion attenuation plot of the 2MP- $\alpha_3\text{C}$  aliphatic protons. For experimental details, see Materials and Methods section in the main text. The data are fitted to Eq. 9 in Ref. S14 and provided a diffusion coefficient of  $1.4 \pm 0.2 \times 10^{-6} \text{ cm}^2 \text{ s}^{-1}$ .

## REFERENCES

- S1. Koradi, R., Billeter, M., and Wüthrich, K. (1996) MOLMOL: A program for display and analysis of macromolecular structures, *J. Mol. Graph.* **14**, 51–52.
- S2. Vuister, G. W., and Bax, A. (1993) Quantitative  $J$  correlation: A new approach for measuring homonuclear three-Bond  $J(\text{H}^{\text{N}}\text{H}^{\alpha})$  coupling constants in  $^{15}\text{N}$ -enriched proteins, *J. Am. Chem. Soc.* **115**, 7772–7777.
- S3. Berjanskii, M. V., and Wishart, D. S. (2005) A simple method to predict protein flexibility using secondary chemical shifts, *J. Am. Chem. Soc.* **127**, 14970–14971.
- S4. Bard, A. J., and Faulkner, L. R. (2001) *Electrochemical methods: Fundamentals and applications*, 2nd Ed., John Wiley & Sons, Inc., USA.
- S5. Osteryoung, J., and O'Dea, J. J. (1986) Square-wave voltammetry, in *Electroanalytical chemistry* (Bard A. J., Ed.) **5**, pp 209–308, Marcel Dekker, New York.
- S6. Mirčeski, V., Komorsky-Lovrić, Š., and Lovrić, M. (2007) Square-wave voltammetry: Theory and applications, in *Monographs in electrochemistry* (Scholz. F., Ed.) Springer-Verlag, Berlin, Germany.
- S7. Blanford, C. F., and Armstrong, F. A. J. (2006) *Solid State Electrochem.* **10**, 826–832.
- S8. McCreery, R. L. (2008) Advanced carbon electrode materials for molecular electrochemistry, *Chem. Rev.* **2008**, **108**, 2646–2687.
- S9. Parry, E. P., and Osteryoung, R. A. (1965) Evaluation of analytical pulse polarography, *Anal. Chem.* **37**, 1634–1637.
- S10. Hay, S., Westerlund, K., and Tommos, C. (2005) Moving a phenol hydroxyl group from the surface to the interior of a protein: Effects on the phenol potential and  $\text{pK}_{\text{A}}$ , *Biochemistry* **44**, 11891–11902.
- S11. Ralph, T. R., Hitchman, M. L., Millington, J. P., and Walsh, F. C. (1994) The electrochemistry of L-cystine and L-cysteine: part 1: thermodynamic and kinetic studies, *J. Electroanal. Chem.* **375**, 1–15
- S12. Martínez-Rivera, M. C., Berry, B. W., Valentine, K. G., Westerlund, K., Hay, S., and Tommos, C. (2011) Electrochemical and structural properties of a protein system designed to generate tyrosine Pourbaix diagrams, *J. Am. Chem. Soc.* **133**, 17786–17795.
- S13. Jeuken, L. J. C., McEvoy, J. P., and Armstrong, F. A. (2002) Insights into gated electron-transfer kinetics at the electrode-protein interface: A square wave voltammetry study of the blue copper protein azurin, *J. Phys. Chem. B* **106**, 2304–2313.
- S14. Zheng, G., and Price, W.S. (2009) Simultaneous convection compensation and solvent suppression in biomolecular NMR diffusion experiments, *J. Biomol. NMR* **45**, 295–299.